



# Amplification of radially polarized ultra-short pulsed radiation to average output powers exceeding 250 W in a compact single-stage Yb:YAG single-crystal fiber amplifier

Frieder Beirou<sup>1</sup> · Michael Eckerle<sup>1</sup> · Thomas Graf<sup>1</sup> · Marwan Abdou Ahmed<sup>1</sup>

Received: 10 June 2020 / Accepted: 5 August 2020 / Published online: 14 August 2020  
© The Author(s) 2020

## Abstract

A simple and compact single-stage Yb:YAG single-crystal fiber amplifier was setup to amplify 784 fs long seed pulses to an output energy of 6  $\mu$ J and an average output power of 290 W. The experimental results are verified by numerical models to estimate the limitations of the SCF technology with regards to beam quality and average output power.

## 1 Introduction

Radially and azimuthally polarized beams exhibit various advantages for scientific [1] and industrial applications [2–4]. For laser cutting at a wavelength of 1.0  $\mu$ m, it was shown that the feed rate can be increased by 43% using radially polarized beams in comparison to unpolarized beams [2]. Azimuthally polarized ultra-short pulses also proved to be beneficial for the production of micro holes with high aspect ratio, where the machining time was reduced by 50% compared to the application of circularly polarized pulses [3]. The symmetry of the electric field of radially and azimuthally polarized femtosecond pulses furthermore was exploited to manufacture complex biomimetic structures [4]. The potential benefit of radially or azimuthally polarized laser beams led to several scientific reports on different techniques for the generation of these polarization states [5–10]. Figure 1 gives an overview of the state-of-the-art laser systems that generate radially polarized ultra-short pulses (< 10 ps) with average output powers of more than 50 W [11–16].

So far, the highest average power of radially polarized ultra-short pulses was achieved with the thin-disk laser technology [16]. Up to 125 W of average output power was demonstrated with a passively mode-locked thin-disk oscillator [11] and up to 1 kW was shown with a two-stage thin-disk

multipass amplifier (TDMPA) [16]. The low gain of the thin-disk crystal requires a comparatively large number of passes of the seed beam over the thin-disk laser crystal for efficient amplification. This leads to long propagation of the beam inside the amplifier and can affect its stability if no special measures are taken. In contrast, the single-crystal fiber (SCF) technology enables a very compact and simple amplifier setup [17]. With this technology, radially polarized ultra-short pulses were amplified to 85 W [12] and linearly polarized pulses were amplified to 160 W [18]. The aim of the present study was to investigate the capability of this amplifier architecture to scale the average power of beams with radial or azimuthal polarization. A numerical model that allowed us to estimate the output power as well as the beam quality by taking into account thermal effects inside the SCF was developed for this purpose. To experimentally investigate the limitations of power scaling, we used a setup similar to the one described in [19], comprised of a mode-locked thin-disk oscillator and a single SCF amplification stage. Compared to [19], we increased the average seed power by a factor of about 4–53 W and used an SCF with a doping concentration of 1 at% instead of 0.5 at%. As a result this led to an average output power of 290 W, which demonstrates that the SCF technology can be an interesting alternative to TDMPAs for the amplification of radially (and also linearly) polarized pulses to a power level of 300 W at significantly reduced system costs and complexity.

The paper is structured as follows: Sect. 2 describes the numerical model to estimate the output power and beam quality that can be expected with the available pump power (1 kW) and seed power (53 W). The experimental setup as well as the experimental results are described in Sects. 3 and

Communicated by Dieter Meschede.

✉ Frieder Beirou  
frieder.beirou@ifsw.uni-stuttgart.de

<sup>1</sup> Institut für Strahlwerkzeuge (IFSW), University of Stuttgart, Pfaffenwaldring 43, 70569 Stuttgart, Germany

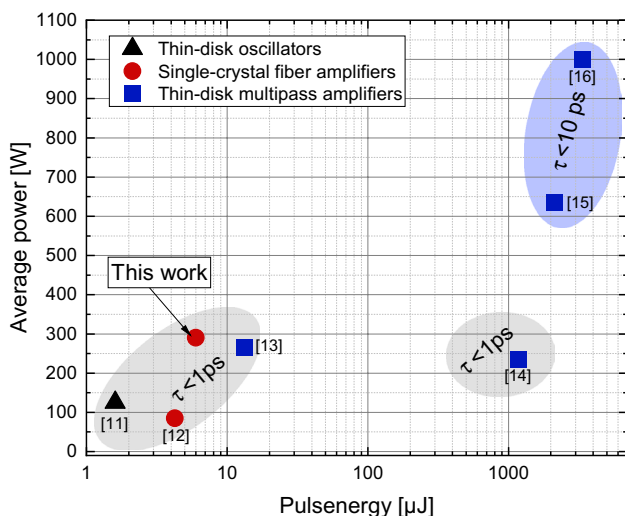


Fig. 1 State-of-the-art ultrafast lasers with radially polarized output

4, respectively. Finally, the experimental results are compared to the simulations in Sect. 5 to predict the possible output power and beam quality that can be obtained by using a more powerful pump and seed source.

## 2 Numerical model

A numerical model that takes into account the distribution of the pump light within the SCF and thermal effects such as the temperature dependence of gain, absorption and refractive index was developed to calculate the output power and beam quality of the amplified beam. The model also considers the dependence of the refractive index on the optical intensity (Kerr lens self-focusing). The temperature dependence of the refractive index leads to thermal lensing as well as to aberrations of higher order. Due to the ring-shaped intensity distribution of the radially polarized  $LG_{01}^*$  mode [20], the Kerr-effect leads to aberrations of higher order and does not contribute to the lensing effect as in the case of a Gaussian beam. A similar model is described in [21] to analyze wavefront distortions of linearly polarized fundamental-mode beams in SCFs but neglecting the temperature dependence of the gain and absorption coefficients as well as the non-linear part of the refractive index. The electric field of an ideal  $LG_{01}^*$  mode with parameters as used in the experiment (waist diameter 0.208 mm located 33 mm in front of the SCF’s entrance facet) was used for the calculations. The distribution of the pump light within the SCF as given by our pumping optics was modeled by means of raytracing (Zemax). For the computation the SCF with a length of 40 mm was split into discrete planes along the longitudinal direction  $z$  with a

distance  $\Delta z$ . For the plane located at  $z_j$ , the amplitude and phase modulation caused by gain and temperature variations was calculated according to [21]

$$E'_j(r) = E_j(r) \cdot e^{-i\varphi_j(r,T,I)} \cdot e^{\frac{g_j(r)}{2} \cdot \Delta z} \tag{1}$$

Here,  $E'_j(r)$  denotes the distribution of the modulated electric field,  $\varphi_j(r, T, I)$  denotes the effective phase modulation,  $g_j(r, z_j)$  denotes the gain coefficient and  $r$  denotes the radial coordinate. The formulas employed to calculate the effective phase modulation and the gain coefficient are given in the appendix. Due to the temperature dependence of the absorption and emission cross sections [22, 23], the gain and absorption coefficients too depend on temperature. To account for this effect, the measured absorption and emission cross sections presented in [22] were fitted as proposed in [23] by taking into account the spectral properties of the pump diode (more details are given in the appendix). After the computation of the effective amplitude and phase modulation in the plane located at  $z_j$ , the modulated electric field  $E'_j(r)$  of the seed beam is propagated to the next plane located at  $z_{j+1}$  by means of Fourier optics with the Fresnel approximation [24, 25]. After one propagation of the seed beam through the SCF, the heat source  $P_{\text{heat}}(r, z)$  inside the SCF is calculated from the absorbed pump power  $P_{\text{abs}}(r, z)$  by taking into account the fractional thermal load  $\eta_{\text{th}}$  [26], which describes the part of absorbed pump light which is converted into heat (for more details see appendix). In addition to the extraction efficiency and the quantum defect, the fractional thermal load depends on the non-radiative quantum efficiency  $\eta_r$ , which represents the amount of excited ions that decay by emission of fluorescence radiation. In [27] the measured non-radiative quantum efficiency was reported to be between 0.898 and 0.932. The spatially varying heat source  $P_{\text{heat}}(r, z)$  is transferred to a finite element analysis (FEA) model using COMSOL Multiphysics to calculate the temperature field  $T(r, z)$  inside the SCF. The calculation of phase and amplitude modulation as well as the beam propagation is repeated, taking into account the previously calculated temperature field  $T(r, z)$ . Due to thermal lensing, the beam diameter inside the SCF changes with each iteration. Consequently, this again leads to a change of the heat source  $P_{\text{heat}}(r, z)$  which, in turn, results in a different temperature field  $T(r, z)$ . The numerical model repeats these iterations until convergence was reached. The beam diameter at the exit facet of the SCF was monitored as a convergence criterion. After typically eight iterations the change of the beam diameter was  $< 0.01\%$ .

To estimate the expected output power and beam quality based on the described model the parameters were set according to the experimental setup, see Table 1. The focal position and waist diameter of the seed beam were

**Table 1** Parameters used for the simulations

Parameter	Value
Seed power	53 W
Pulse repetition rate	48.5 MHz
Pulse duration	830 fs
Max. pump power	1000 W
Pump wavelength	969 nm
Beam waist diameter of the pump beam	600 $\mu\text{m}$
Focal position of the seed beam with regard to the SCF's entrance facet	33 mm
Beam waist diameter of the seed beam	208 $\mu\text{m}$
Doping concentration	1 at. %

varied to find the best performance at maximum pump power. These values were finally used in the experiment.

Since the radiative quantum efficiency  $\eta_r$  and the heat resistance between crystal and heat sink  $R_s$  were not precisely known, a best-case scenario and a worst-case scenario were simulated. In the best-case scenario, the highest quantum efficiency reported in [27] and a perfect thermal contact of crystal and heat sink were assumed ( $\eta_r = 0.932$  and  $R_s = 0 \frac{\text{m}^2\text{K}}{\text{W}}$ ). For the worst-case scenario the lowest quantum efficiency  $\eta_r = 0.898$  reported in [27] and a thermal resistance of  $R_s = 10^{-4} \frac{\text{m}^2\text{K}}{\text{W}}$  between crystal and heat sink were assumed. The thermal resistance between the Yb:YAG laser crystal and the copper heat sink  $R_s$  was discussed in [28] for different contacting techniques, where values ranging between  $R_s = 0.5 \times 10^{-4} \frac{\text{m}^2\text{K}}{\text{W}}$  (thermal contact with heat sink grease) and  $R_s = 4 \times 10^{-4} \frac{\text{m}^2\text{K}}{\text{W}}$  (bare contact with copper heat sink) were reported. The supplier of the used SCF modules specifies the thermal resistance to be  $R_s = 0.2 \times 10^{-4} \frac{\text{m}^2\text{K}}{\text{W}}$  for the latest generation of the modules. Since we were not working with the latest generation, we chose a value of  $R_s = 10^{-4} \frac{\text{m}^2\text{K}}{\text{W}}$  for the worst-case scenario. Figure 2 shows the calculated output power, optical efficiency and beam quality factor  $M^2$  for the best-case scenario (black symbols) and the worst-case scenario (red symbols), respectively. Consequently, an output power in the range of 240–360 W can be expected. However, as can be seen in Fig. 2c), the beam quality decreases significantly with increasing output power. A good beam quality ( $M^2 < 2.5$ ) can be expected for output powers of up to 240 W, assuming the best-case scenario and 200 W, assuming the worst-case scenario. The highly degraded beam quality calculated for low pump powers can be attributed to diffraction of the diverging seed beam at the crystal's exit aperture. Due to thermal lensing, the seed beam becomes smaller at the exit aperture with increasing pump power, resulting in a higher beam quality.

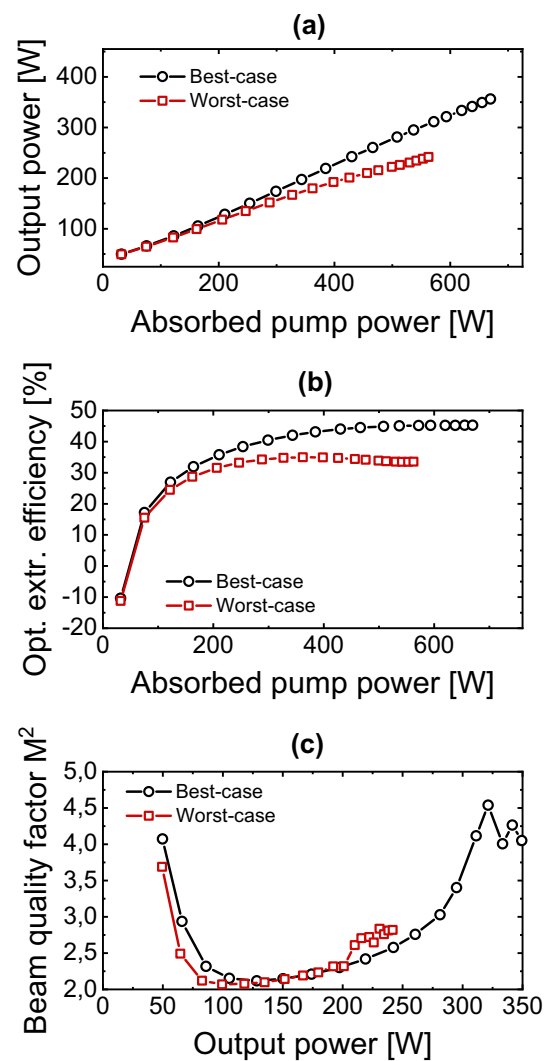


**Fig. 2** a Calculated output power versus absorbed pump power, b calculated optical extraction efficiency versus absorbed pump power and c calculated beam quality factor  $M^2$  versus output power for the best-case scenario ( $\eta_r = 0.932$  and  $R_s = 0 \frac{\text{m}^2\text{K}}{\text{W}}$ ) and for the worst-case scenario ( $\eta_r = 0.898$  and  $R_s = 10^{-4} \frac{\text{m}^2\text{K}}{\text{W}}$ ), respectively

### 3 Experimental setup

#### 3.1 Seed laser

A passively mode-locked thin-disk oscillator similar to the one presented in [11] was used to seed the SCF with radially polarized ultra-short pulses. A Semiconductor Saturable Absorber Mirror (SESAM) was implemented as cavity end-mirror to stabilize soliton mode-locking and a Grating Waveguide Output coupler was used to select the radially polarized  $LG_{01}^*$  mode. In contrast to [11], this oscillator was pumped at a wavelength of 940 nm. To reduce thermal effects, a thinner Yb:YAG crystal with a higher doping concentration than in [11] was used (thickness of 110  $\mu\text{m}$

and 11 at.% doping). The oscillator delivered an average power of 53 W at a repetition rate of 48.5 MHz. The pulse duration of the seed pulses was 784 fs and the spectral bandwidth amounted to 1.56 nm, resulting in a close to transform limited time-bandwidth product of 0.345. The measured autocorrelation trace, spectral intensity and the pulse train are shown in Fig. 3.

The beam quality factor  $M^2$  of the seed beam was measured to be  $< 2.3$  and the polarization purity was analyzed qualitatively by a rotating polarizer in front of a camera. Figure 4 shows the intensity distribution recorded behind the polarizer for different orientation angles (indicated by the white arrows). The well separated lobes indicate a high degree of radial polarization (which is typically  $> 95\%$ ).

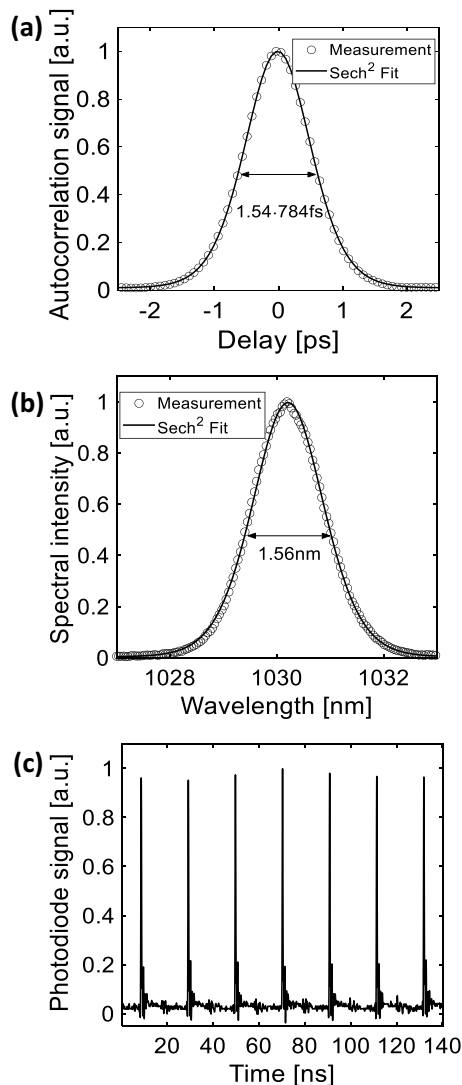
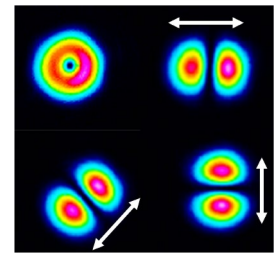


**Fig. 3** **a** Measured autocorrelation trace, **b** measured spectral intensity and **c** pulse train of the seed laser

**Fig. 4** Qualitative polarization analysis



### 3.2 Single-crystal fiber amplifier

The SCF used in this experiment had a length of 40 mm, a diameter of 1 mm and the doping concentration was 1 at.%. Significant thermal lensing of SCFs was observed in previous experiments [19]. The seed beam was therefore injected with a slight divergence into the SCF to avoid a tight focus at the exit facet and to maximize the overlap with the pump beam (Fig. 5).

A spherical mirror with a radius of curvature of 750 mm was used to focus the seed beam to a location approximately 33 mm in front of the SCF. The focal diameter was measured to be 208  $\mu\text{m}$  and the beam diameter at the entrance facet of the SCF was measured to be 465  $\mu\text{m}$ . To reduce the pump-induced heat load, the SCF was pumped at the zero-phonon line [29] of Yb:YAG by a fiber-coupled laser diode emitting at a wavelength of 969 nm. The beam leaving the pump fiber with a diameter of 600  $\mu\text{m}$  was imaged to plane at 1 mm in front of the SCF's entrance facet by two aspheric lenses with a focal length of 80 mm. The seed beam and the pump beam were first combined and then separated by a pair of dichroic mirrors. The pump radiation that was not absorbed in the single pass through the SCF was dumped on a power head. To preserve the radial polarization of the seed laser, it was necessary to implement a variable phase retarder in the beam path in front of the SCF to pre-compensate for a power-dependent linear phase shift between s- and p-polarization

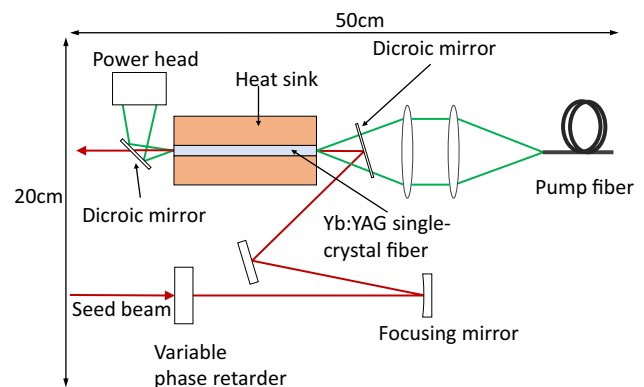


**Fig. 5** Experimental setup for the amplification in a Yb:YAG single-crystal fiber

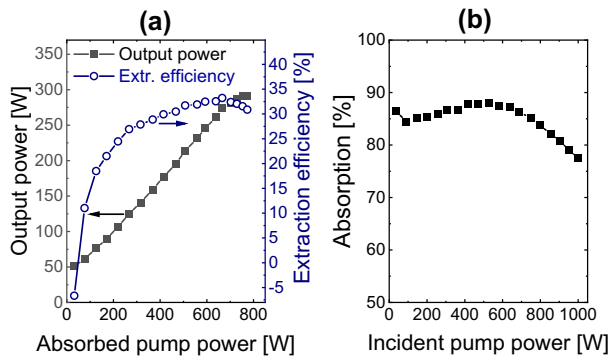


**Fig. 6** **a** Output power and extraction efficiency versus absorbed pump power. **b** Absorption of pump power versus incident pump power

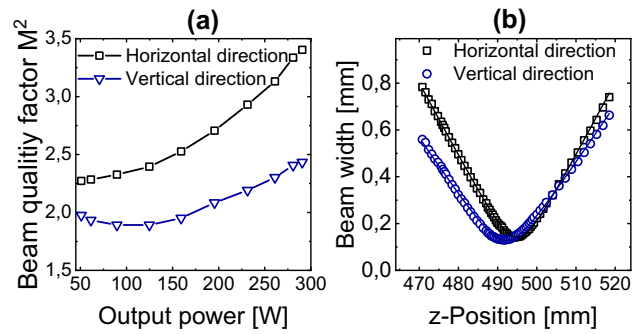
inside of the amplifier crystal. This phase shift can be attributed to stress induced birefringence inside the crystal which increases with the thermal load. The retardation between s- and p-polarization had to be adapted for each power level to ensure pure radial polarization of the amplified beam.

### 4 Experimental results

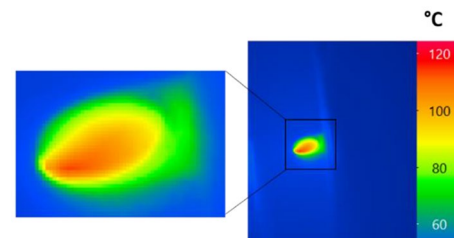
Figure 6a shows the extracted output power and the optical extraction efficiency versus absorbed pump power, and Fig. 6b depicts the absorption of the pump power as a function of the incident pump power. At an incident pump power of 1 kW, an average output power of 290 W was obtained. The corresponding pulse energy and pulse peak power was 6  $\mu$ J and 6.4 MW, respectively. The maximum extraction efficiency of 33.2% with respect to the absorbed pump power was reached at an output power of 274 W (666 W of absorbed pump power). At the maximum output power of 290 W, the extraction efficiency dropped to 30.9%. The absorption of the pump power in the SCF decreased from 86.5% at 37 W of incident pump power to 77.5% at 1 kW of incident pump power.

Figure 7 shows the beam quality factor  $M^2$  measured according to ISO 11145 as a function of the output power. As can be seen from Fig. 7a the beam quality is less affected along the vertical direction. In fact, the stronger degradation of the beam quality along the horizontal axis can be attributed to a higher temperature gradient along this direction, as can be seen in the thermography image of the SCF's entrance facet shown in Fig. 8.

At the maximum output power of 290 W, a beam quality factor of 2.4 and 3.4 was measured along the vertical and horizontal direction, respectively. Figure 7b shows the measured caustic (beam width measured with the second moment method) at the maximum output power. The far-field intensity distribution is shown in Fig. 9a.

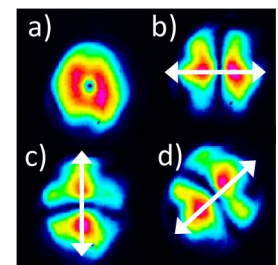


**Fig. 7** **a** Beam quality factor  $M^2$  over output power. **b** Beam caustic at 290 W of output power



**Fig. 8** Thermography image of the SCF's entrance facet at 1 kW of incident pump power

**Fig. 9** **a** Far-field intensity distribution. **b-d** Far-field intensity distribution behind polarization analyzer at different angles indicated by white arrows



The polarization purity of the amplified beam was analyzed qualitatively by implementing a rotatable polarizer into the diagnostic beam path. Figure 9b-d show the recorded intensity distribution for different angles of the polarizer, indicated by white arrows. The clearly separated intensity lobes aligned along the transmission axis of the polarizer indicate a high radial polarization purity.

Figure 10a, b show the measured autocorrelation trace and spectral intensity at 290 W of output power. The measured pulse duration was 829 fs and the spectral full-width at half maximum was 1.43 nm, resulting in a time-bandwidth-product of 0.326 and indicating almost transform-limited pulses.

To summarize, we amplified ultra-short radially polarized pulses to an average output power of 290 W with a beam quality factor of 2.4 and 3.4 along the vertical and horizontal



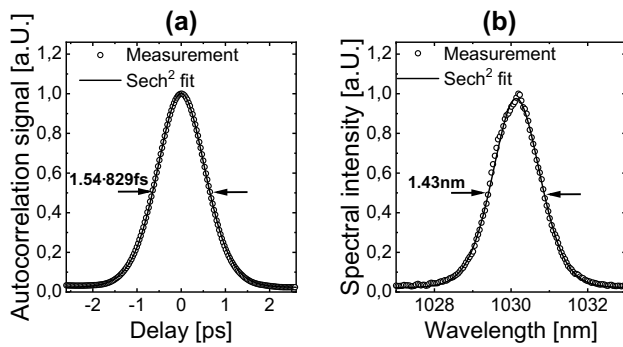


**Fig. 10** **a** Normalized autocorrelation signal and **b** normalized spectral intensity at 290 W of output power

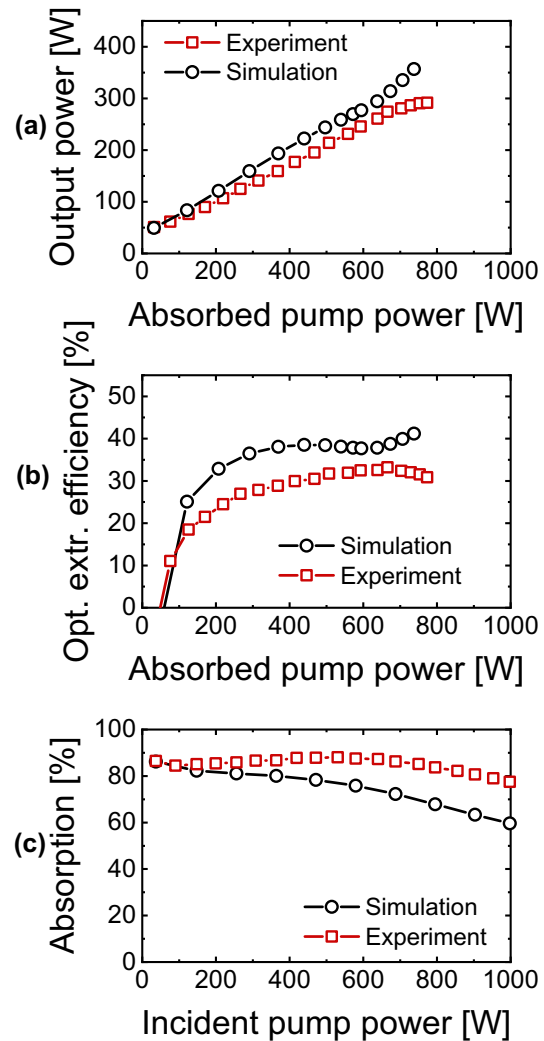
direction, respectively. Significantly higher beam quality could be obtained with laser amplifier systems based on the thin-disk technology [13, 15] for even higher average powers of up to 635 W. However, this improvement comes at the cost of complexity, footprint size and overall costs of the laser system.

## 5 Discussion

To fit the simulation more precisely to the experimental results, rather than just using the two scenarios mentioned in Sect. 2, both the radiative quantum efficiency  $\eta_r$  and the thermal resistance  $R_s$  between crystal and heat sink were adapted and used as fitting parameters.

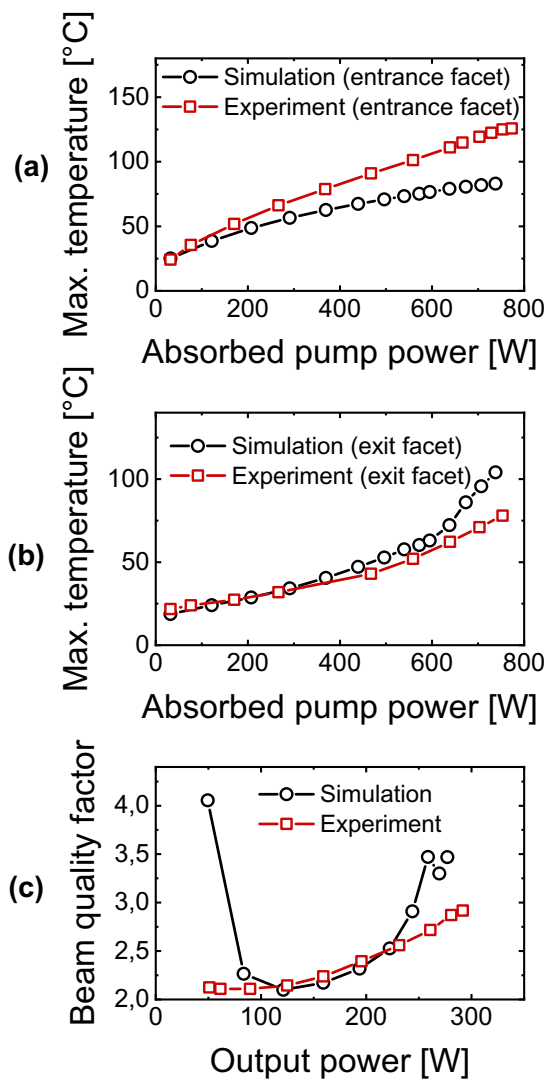
The best agreement between the numerical model and the experimental data was obtained by setting the radiative quantum efficiency to  $\eta_r = 0.932$  and the heat resistance between crystal and heatsink to  $R_s = 10^{-4} \frac{\text{m}^2\text{K}}{\text{W}}$ . Figure 11 shows a comparison of the experimental data and the data obtained from the numerical model with the abovementioned parameters. As can be seen from Fig. 11a, b, both the calculated output power and the calculated optical extraction efficiency are slightly higher than the measured values. This can be explained by additional losses due to imperfections in the crystal. The slightly increasing extraction efficiency calculated for absorbed pump powers in excess of 600 W can be attributed to an increased overlap between seed and pump beams. Experimentally, this behavior was not observed, indicating a slightly different thermally induced lens inside the crystal. The calculated absorption at 1 kW of incident pump power is 17% lower than the measured absorption, most likely due to a higher actual doping concentration of the SCF than the specified value of 1 at%.

Figure 12a, b show the calculated and the measured maximum temperature of the SCF's entrance and exit facet. The calculated temperature of the entrance facet is significantly lower than the measured one, whereas the calculated and measured temperature of the exit facet are in good agreement. As observed with the absorption, the difference of the



**Fig. 11** Comparison between simulation ( $\eta_r = 0.932$ ,  $R_s = 10^{-4} \frac{\text{m}^2\text{K}}{\text{W}}$  and doping concentration 1 at%) and experiment. **a** Output power versus absorbed pump power, **b** optical extraction efficiency versus absorbed pump power and **c** absorption versus incident pump power

higher measured temperature indicates a higher than specified doping of the SCF. A higher doping concentration of the crystal results in a higher amount of absorbed pump power at the entrance facet and a lower amount of absorbed pump power at the exit facet. As a result, an increased doping concentration leads to a higher temperature at the entrance facet and a lower temperature at the exit facet. Figure 12c shows the measured as well as the calculated beam quality factor (mean value of horizontal and vertical direction of the values shown in Fig. 7b) as a function of the output power. For output powers < 100 W, the model predicts a highly degraded beam quality as a result of diffraction of the seed beam at the SCF's exit facet. However, no beam quality degradation at low output power was observed in the experiment. We therefore conclude that the thermal lensing inside the SCF,



**Fig. 12** Comparison between simulation ( $\eta_r = 0.932$ ,  $R_s = 10^{-4} \frac{m^2 K}{W}$ ) and experiment. **a** Beam quality factor  $M^2$ , **b** maximum temperature of the entrance facet and **c** maximum temperature of the exit facet

which reduces the beam diameter at the SCF's exit facet, was stronger in the experiment compared to the one considered in the numerical model. This effect can again be attributed to a higher doping concentration of the SCF.

Based on the numerical model, the potential of further average and peak power scaling using the SCF technology is discussed in the following. The parameters that led to the best agreement between simulation and experiment ( $\eta_r = 0.932$  and  $R_s = 10^{-4} \frac{m^2 K}{W}$ ) were used for this purpose. In order to estimate the potential performance of the SCF technology for the scaling of the average power, a continuous-wave seed beam with different powers of up to 500 W was considered. Consequently, the degradation of the beam quality caused by the non-linear contribution to the refractive index was

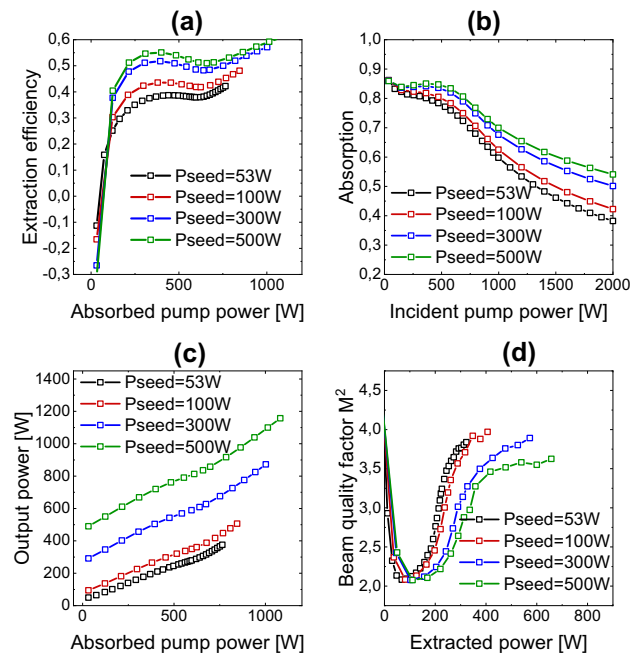


**Fig. 13** Investigation of the scaling of the average power using the numerical model with  $\eta_r = 0.932$  and  $R_s = 10^{-4} \frac{m^2 K}{W}$  for incident pump powers up to 2 kW and different seed powers (continuous wave) up to 500 W. **a** Output power vs. absorbed pump power, **b** pump light absorption vs. incident pump power, **c** optical extraction efficiency vs. absorbed pump power and **d** beam quality factor as a function of extracted optical power

neglected. Figure 13 shows the results calculated for incident pump powers of up to 2 kW. At an incident pump power of 2 kW and a seed power of 53 W, the model predicts an output power of 375 W with a beam quality factor of 3.84. The calculated absorption of the pump power significantly drops to about 40% at this power level. Consequently, a higher seed power is required to increase the absorption of the pump light and the output power for incident pump powers in excess of 1 kW. Assuming a seed power of 500 W (which might be available from a mode locked thin-disk oscillator in the near future [30]), the numerical model predicts an output power exceeding 1 kW at an incident pump power of 2 kW. The beam quality calculated at this power level amounts to 3.63 and the calculated absorption of the pump radiation is 54%.

To investigate the potential with respect to the pulse peak power imposed by the non-linear contribution to the refractive index (Kerr-lens self-focusing), the pulse repetition rate was varied at a fixed incident pump power and seed power. The black symbols in Fig. 14 show the evolution of the beam quality with increasing peak power of the pulses at an average power of 120 W (250 W incident pump power and 53 W seed power). At pulse peak powers exceeding 10 MW, the beam quality starts to degrade rapidly. The red symbols in Fig. 14 show the evolution of the beam quality at an average output power of 280 W (1 kW incident pump

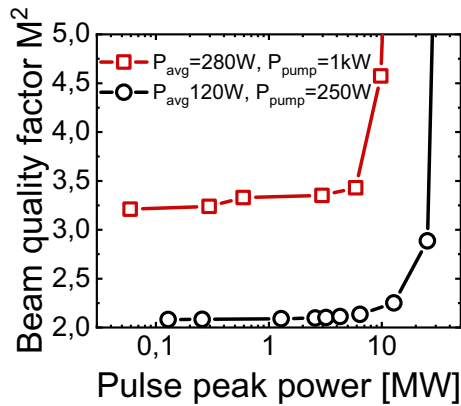


**Fig. 14** Variation of the pulse peak power at two fixed pump and seed power levels

power and 53 W seed power). Due to the tighter focus inside the SCF caused by the thermal lens at this power level, the degradation of the beam quality caused by the non-linear contribution to the refractive index starts at slightly lower peak powers of the pulse of around 8 MW. Consequently, the numerical model indicates that the obtainable pulse peak power is limited to approximately 8 MW. At this peak power, the energy density at the SCF's exit facet is significantly below the damage threshold of about  $1.1 \text{ J/cm}^2$  [17] for pulses with a duration of around 1 ps.

To summarize, the numerical model clearly shows that the average output power with good beam quality ( $M^2 < 2.5$ ) is limited to 240 W assuming a seed power of 53 W. Furthermore, the numerical model suggests that further power scaling towards the kW-level is feasible at the cost of a reduced beam quality ( $M^2 > 3.5$ ) when higher seed powers and pulse peak powers below 8 MW are applied. Hence, for applications that tolerate a degraded beam quality (up to  $M^2 = 4$ ), the SCF technology might be an interesting approach to amplify radially polarized pulses at GHz repetition rates towards the kW power level for efficient material removal [31].

## 6 Conclusion

In conclusion, we demonstrated for the first time, to the best of our knowledge, the amplification of sub-picosecond pulses up to an average output power of 290 W with a compact single-stage SCF amplifier. The experimental results indicate that there is still room for improvement concerning the mounting technology of the SCF to achieve a symmetric heat flow, which will result in a more symmetric output beam.

The numerical model that was developed to investigate the potential for further power scaling of radially polarized beams with the SCF technology predicts that the output power from a single-stage SCF amplifier with good

beam quality ( $M^2 < 2.5$ ) is limited to 240 W assuming a seed power of 53 W. The numerical model suggests that power scaling towards the kW-level is possible by injecting a significantly higher seed power of 500 W with a pulse peak power  $< 8 \text{ MW}$  when a reduced beam quality ( $M^2 > 3.5$ ) can be accepted. To sum up, our experimental investigations showed that the SCF technology represents a simple, compact and cost efficient alternative to the thin-disk multipass technology for output powers up to 250 W. Moreover, a single-stage SCF amplifier can be used as pre-amplifier in front of a thin-disk multipass amplifier to scale the average power toward 2 kW or even more.

**Acknowledgements** The authors thank the company Fibercryst, Xavier Delèn, Philipp Albrodt, Francois Balembois and Patrick Georges from the Laboratoire Charles Fabry Intitut d'Optique for the fruitful discussions.

**Funding** Open Access funding provided by Projekt DEAL.

**Open Access** This article is licensed under a Creative Commons Attribution 4.0 International License, which permits use, sharing, adaptation, distribution and reproduction in any medium or format, as long as you give appropriate credit to the original author(s) and the source, provide a link to the Creative Commons licence, and indicate if changes were made. The images or other third party material in this article are included in the article's Creative Commons licence, unless indicated otherwise in a credit line to the material. If material is not included in the article's Creative Commons licence and your intended use is not permitted by statutory regulation or exceeds the permitted use, you will need to obtain permission directly from the copyright holder. To view a copy of this licence, visit <http://creativecommons.org/licenses/by/4.0/>.

## Appendix

### Calculation of the effective phase modulation

As a result of thermal dispersion and the non-linear response of the medium to high optical intensities, the refractive index of the SCF crystal depends on the temperature field  $T(r, z)$  as well as on the optical intensity  $I(r, z)$ . The resulting phase modulation experienced by the electric field after propagation from one plane located at  $z_j$  to the next plane located at a distance of  $\Delta z$  was calculated as follows [23, 32]:

$$\varphi_j(r, T, I) = \frac{2\pi}{\lambda_L} \cdot \left( \left( \frac{dn}{dT} + (n_0 - 1) \cdot \alpha_{th} \right) \cdot T(r, z_j) + \Delta n_r \right) \cdot \Delta z + \frac{2\pi}{\lambda_L} n_2 \cdot I(r, z_j) \cdot \Delta z. \quad (2)$$

Here,  $\lambda_L$ ,  $\frac{dn}{dT}$ ,  $n_0$ ,  $\alpha_{th}$ ,  $\Delta n_r$  and  $n_2$  denote the laser wavelength, the thermal dispersion coefficient, the initial refractive index, the thermal expansion coefficient, the stress induced change of the refractive in radial direction and the second order non-linear refractive index, respectively.



### Calculation of gain and absorption coefficients

The steady-state absorption coefficient for the pump beam  $\alpha_p(r, z_j)$  and the gain coefficient for the seed beam  $g_l(r, z_j)$  in the plane located at  $z_j$  were calculated according to [32]

$$\alpha_p(r, z_j) = \frac{I_l(r, z_j) \cdot N \cdot \tau [\alpha_{\text{abs}}(\lambda_p, T)\sigma_{\text{em}}(\lambda_l, T) - \sigma_{\text{abs}}(\lambda_l, T)\sigma_{\text{em}}(\lambda_p, T)] + \sigma_{\text{abs}}(\lambda_p, T) \cdot N}{\left(1 + \frac{I_p(r, z_j)}{I_{p,\text{sat}}} + \frac{I_l(r, z_j)}{I_{l,\text{sat}}}\right)} \tag{3}$$

$$g_l(r, z_j) = \frac{I_p(r, z_j) \cdot N \cdot \tau [\alpha_{\text{abs}}(\lambda_p, T)\sigma_{\text{em}}(\lambda_l, T) - \sigma_{\text{abs}}(\lambda_l, T)\sigma_{\text{em}}(\lambda_p, T)] - \sigma_{\text{abs}}(\lambda_l, T) \cdot N}{\left(1 + \frac{I_p(r, z_j)}{I_{p,\text{sat}}} + \frac{I_l(r, z_j)}{I_{l,\text{sat}}}\right)} \tag{4}$$

Here,  $I_l(r, z_j), I_p(r, z_j), I_l(\text{sat}), I_p(\text{sat}), \sigma_{\text{abs}}(\lambda_p, T), \sigma_{\text{em}}(\lambda_p, T), \sigma_{\text{abs}}(\lambda_l, T), \sigma_{\text{em}}(\lambda_l, T)$  and  $N$  denote the laser intensity, the pump intensity, the laser saturation intensity, the pump saturation intensity, the absorption cross section for the pump beam, the emission cross section for the pump beam, the absorption cross section of the seed beam, the emission cross section of the seed beam and the density of laser active ions, respectively. To take into account the temperature dependence of the absorption and emission cross sections, the measurement values given in [22] were fitted as proposed in [23]. Furthermore, the power-dependent spectral properties of the pump source were taken into account for the calculation of the absorption and emission cross section for the pump radiation. Table 2 shows the parameters used to calculate the absorption and gain coefficients.

### Calculation of the fractional thermal load

According to [26], the fractional thermal load which describes the part of the absorbed power that is converted into heat is calculated as follows (Fig. 15):

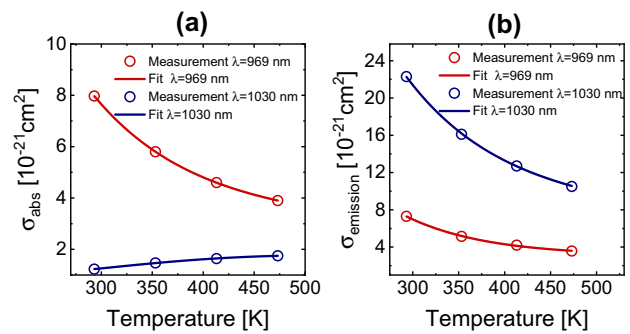


**Fig. 15** **a** Temperature dependent absorption cross section for pump and seed beam. **b** Temperature dependent emission cross section for pump and seed beam. The measured values are taken from [22]

**Table 2** Material parameters of Yb:YAG used to calculate the absorption and gain coefficient

Parameter	Symbol	Value	References
Pump wavelength	$\lambda_p$	969 nm	
Laser wavelength	$\lambda_l$	1030 nm	
Absorption cross section	$\sigma_{\text{abs}}(\lambda_p, T)$	$e^{-0.005K^{-1} \cdot T} (79.68 - 0.27 \cdot T + 4.01 \cdot 10^{-4} \cdot T^2) \times 10^{-25} \text{ m}^2$	[22, 23]
<i>Pump beam</i>			
Emission cross section	$\sigma_{\text{em}}(\lambda_p, T)$	$e^{-0.005K^{-1} \cdot T} (87.59 - 0.33 \cdot T + 4.84 \times 10^{-4} \cdot T^2) \times 10^{-25} \text{ m}^2$	[22, 23]
<i>Pump beam</i>			
Absorption cross section	$\sigma_{\text{abs}}(\lambda_l, T)$	$e^{-0.005K^{-1} \cdot T} (6.67 - 0.05 \cdot T + 1.65 \times 10^{-4} \cdot T^2) \times 10^{-25} \text{ m}^2$	[22, 23]
<i>Seed beam</i>			
Emission cross section	$\sigma_{\text{em}}(\lambda_l, T)$	$e^{-0.005K^{-1} \cdot T} (207.81 - 0.67 \cdot T + 9.9 \times 10^{-4} \cdot T^2) \times 10^{-25} \text{ m}^2$	[22, 23]
<i>Seed beam</i>			
Lifetime of excited level	$\tau$	951 $\mu\text{s}$	[20]
Active laser ion density	$N$	$1.38 \times 10^{26} \text{ m}^{-3}$	[20]

$$\eta_{th} = 1 - \eta_p \left[ (1 - \eta_l) \eta_r \frac{\lambda_p}{\lambda_f} + \eta_l \frac{\lambda_p}{\lambda_l} \right]. \quad (5)$$

Here,  $\lambda_p$ ,  $\lambda_f$ ,  $\lambda_l$  denote the pump wavelength (969 nm), the average fluorescence wavelength (1008 nm) and the laser wavelength (1030 nm), respectively. Furthermore,  $\eta_p$  denotes the pump quantum efficiency, which describes the part of pump photons that contribute to inversion. In the simulations, we assumed a pump quantum efficiency of unity.  $\eta_l$  denotes the laser extraction efficiency which is the ratio of extracted laser power to absorbed pump power. Finally,  $\eta_r$  denotes the radiative quantum efficiency for the upper manifold, which describes the part of excited ions that decay by emission fluorescence radiation.

## References

- Q. Zhan, *Ad. Opt. Photon.* **1**, 1 (2009)
- T. Häcker, In *AKL International Laser Technology Congress* (2016)
- M. Kraus, M.A. Ahmed, A. Michalowski, A. Voss, R. Weber, T. Graf, *Opt. Express* **18**, 21 (2010)
- E. Skoulas, A. Manousaki, C. Fotakis, E. Stratakis, *Sci. Rep.* **7**, 20 (2017)
- M.A. Ahmed, A. Voss, M.M. Vogel, T. Graf, *Opt. Lett.* **32**, 22 (2007)
- G. Machavariani, Y. Lumer, I. Moshe, A. Meir, S. Jackel, N. Davidson, *Appl. Opt.* **46**, 16 (2007)
- I. Moshe, S. Jackel, A. Meir, *Opt. Lett.* **28**, 10 (2003)
- A. Ito, Y. Kozawa, S. Sato, *J. Opt. Soc. Am. B* **26**, 4 (2009)
- S. Quabis, R. Dorn, G. Leuchs, *Appl. Phys. B Lasers Opt.* **81**, 5 (2005)
- M. Beresna, M. Gecevičius, P.G. Kazansky, T. Gertus, *Appl. Phys. Lett.* **98**, 20 (2011)
- F. Beirou, M. Eckerle, B. Dannecker, T. Dietrich, M.A. Ahmed, T. Graf, *Opt. Express* **26**, 4 (2018)
- F. Lesparre, J.T. Gomes, X. Délen, I. Martial, J. Didierjean, W. Pallmann, B. Resan, M. Eckerle, T. Graf, M.A. Ahmed, F. Druon, F. Balembois, P. Georges, *Opt. Lett.* **40**, 11 (2015)
- A. Loescher, J.-P. Negel, T. Graf, W. Pallmann, B. Resan, I. Martial, J. Didierjean, F. Lesparre, J.-T. Gomes, X. Délen, F. Druon, F. Balembois, P. Georges, M.A. Ahmed, M.A. Ahmed, *Adv. Solid State Lasers* **20**, ATh3A.3.OSA (2015)
- J.-P. Negel, A. Loescher, B. Dannecker, P. Oldorf, S. Reichel, R. Peters, M.A. Ahmed, T. Graf, *Appl. Phys. B* **123**, 5 (2017)
- A. Loescher, J.-P. Negel, T. Graf, M.A. Ahmed, *Opt. Lett.* **40**, 24 (2015)
- A. Loescher, J.-p. Negel, . Röcker, F. Beirou, T. Graf, Thin-disk multipass amplifier delivering radially polarized ultrafast pulses with an average output power of 1 kW. volume 2016, p. 7281 (2019)
- X. Délen, Y. Zaouter, I. Martial, N. Aubry, J. Didierjean, C. Hönniger, E. Mottay, F. Balembois, P. Georges, *Opt. Lett.* **38**, 2 (2013)
- V. Markovic, A. Rohrbacher, P. Hofmann, W. Pallmann, S. Pierrot, B. Resan, *Opt. Express* **23**, 20 (2015)
- M. Eckerle, F. Beirou, T. Dietrich, F. Schaal, C. Pruss, W. Osten, N. Aubry, M. Perrier, J. Didierjean, X. Délen, F. Balembois, P. Georges, M.A. Ahmed, T. Graf, *Appl. Phys. B* **123**, 5 (2017)
- W. Koehnner, *Solid-State Laser Engineering* (Springer, New York, 2006)
- P. Albrodt, X. Delen, M. Besbes, F. Lesparre, P. Georges, *J. Opt. Soc. Am. B* **35**, 12 (2018)
- J. Koerner, C. Vorholt, H. Liebetrau, M. Kahle, D. Kloepfel, R. Seifert, J. Hein, M.C. Kaluza, *J. Opt. Soc. Am. B* **29**, 9 (2012)
- K. Contag, *Modellierung und Numerische Auslegung des Yb:YAG-Scheibenlasers*. PhD thesis, University of Stuttgart (2002)
- J.D. Schmidt, *SPIE* (2010)
- A.E. Siegman, *Lasers* (University Science Books, California, 1986)
- T.Y. Fan, *IEEE J. Quant. Electron.* **29**, 6 (1993)
- N. Barnes, B.M. Walsh, *Adv. Solid State Lasers* **68**, 20 (2002)
- S. Chénais, F. Druon, S. Forget, F. Balembois, P. Georges, *Progress Quant. Electron.* **30**, 4 (2006)
- B. Weichelt, A. Voss, M.A. Ahmed, T. Graf, *Opt. Lett.* **37**, 15 (2012)
- F. Saltarelli, I.J. Graumann, L. Lang, D. Bauer, C.R. Phillips, U. Keller, *Opt. Express* **27**, 22 (2019)
- C. Kerse, H.K. Lu, P. Elahi, B. Çetin, D.K. Kesim, Ö. Akçaalan, S. Yavaş, M.D. Aşlk, B. Öktem, H. Hoogland, R. Holzwarth, F.Ö. Ilday, *Nature* **537**, 7618 (2016)
- Sa. Damien, PhD thesis, University Lyon (2009)

**Publisher's Note** Springer Nature remains neutral with regard to jurisdictional claims in published maps and institutional affiliations.